International Journal of Pharmaceutics 377 (2009) 45–51

Contents lists available at ScienceDirect

International Journal of Pharmaceutics

journal homepage: www.elsevier.com/locate/ijpharm

Numerical calibration of the Andersen cascade impactor using a single jet model

Yuriy Gulak[a], Eric Jayjock[a], Fernando Muzzio[a,*], Andrea Bauer[b], Paul McGlynn[b]

[a] Dept. of Chemical and Biochemical Engineering, Rutgers University, 98 Brett Road, Piscataway, NJ 08854-8058, United States
[b] Sepracor, United States

ARTICLE INFO

Article history:
Received 13 February 2009
Received in revised form 16 April 2009
Accepted 29 April 2009
Available online 21 May 2009

Keywords:
Andersen cascade impactor (ACI)
Single jet model
d_{50}
Cutoff diameter

ABSTRACT

A single jet model is described and used to analyze the performance of an 8-stage Andersen cascade impactor (ACI). The two-dimensional axisymmetric jet flow field was calculated numerically by solving the Navier–Stokes equations and particle trajectories were then analyzed to obtain the collection efficiency curves at different flow rates. The resulting efficiency curves and corresponding cutoff diameters were compared and found to be in good agreement with the available experimental data. We also examined the effect of gravity on impactor performance and discuss the limitations of the single jet model.

1. Introduction

The delivery of active ingredients through the pulmonary pathway has received considerable attention in the past 10 years. The large surface area and relatively quick uptake time make the lungs an attractive pathway for drug delivery. In recent years, researchers have focused on delivering dry powder aerosol particles to the lungs. It is well understood that in this mode of drug delivery, the particle size distribution of the active aerosol determines the success or failure of the drug delivery approach. This creates the need for tools to accurately and efficiently measure the particle size distribution being emitted from a delivery device.

Currently, one of the most commonly used devices to characterize aerosol size distribution is an 8-stage Andersen cascade impactor (ACI). Cascade impactors, first introduced by May (1945), use the particle inertia in a jet directed normally toward a collection surface (Fig. 1).

The larger particles with higher momentum collide with the collection surface, while smaller particles escape. The ACI is designed to impinge air onto a metal collection plate at increasing velocities as the air travels through the impactor. In the initial stages of the impactor, the velocity is lowest; only larger particles with high momentum impact on the collection plates. As the velocity of the air impinging on the surface increases, particle momentum increases and hence smaller particles are collected. The plates can then be weighed to determine the mass of impacted particles and the particle size distribution is estimated, provided the collection efficiency curve (percentage of retained particles vs. particle size) is known for each stage.

The collection efficiency data as well as the 50% effective cutoff aerodynamic diameters (d_{50}) are usually available from the ACI manufacturer's calibrations, typically performed at a 28.3 liter per minute (lpm) air flow rate (the base case). Furthermore, the results of extensive experimental studies and the calibration of the ACI operated at the 28.3 lpm flow rate were reported in Mitchell et al. (1988) and Vaughan (1989). Recently, however, ACI have been used at flow rates considerably different from 28.3 lpm, which required a corresponding re-calibration of the impactor. Thus, Zhou et al. (2007) employed the ACI to evaluate a nebulizer at an 18.0 lpm flow rate. The impactor was calibrated with mono-disperse fluorescent test particles. In a similar study Nichols et al. (1998) measured retention curves at 60 lpm. Separately, Srichana et al. (1998) used a different calibration technique to measure flows at both 60 and 28 lpm.

The theoretical prediction of the efficiency and cutoff diameters, however, is more complex due to the multi-scale geometry and aerodynamics of the ACI. Earlier models were based on studies of impaction in plane stagnation flows (Ranz and Wong, 1952; Mercer and Stafford, 1968) or ideal fluid potential flows (Davies and Alyward, 1951), in which analytical expressions for the velocity field could be obtained. Despite their simplicity, such models provided an adequate physical description and outlined the importance of various mechanisms on the impaction. In the early-1970s the application of digital computing leads to a more detailed understanding of impactor design (Marple and Willeke, 1976). It should be noted that the ACI, being designed prior to the Marple work, does not strictly follow design recommendation; most notable the ACI is typically operated to with Reynolds numbers ranging from 50

* Corresponding author.
E-mail address: fjmuzzio@yahoo.com (F. Muzzio).

0378-5173/$ – see front matter © 2009 Elsevier B.V. All rights reserved.
doi:10.1016/j.ijpharm.2009.04.051

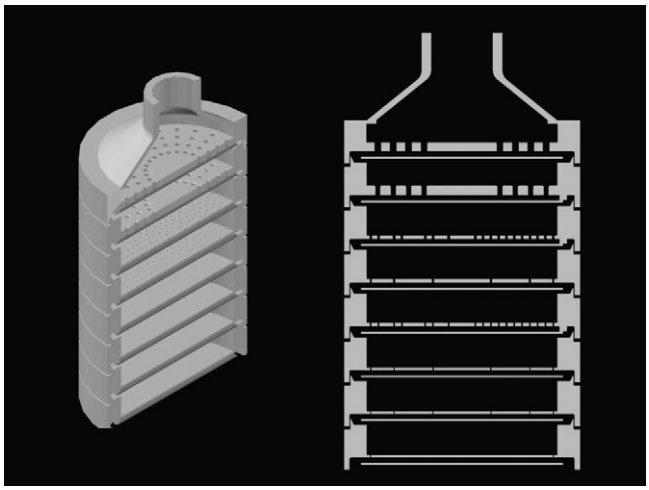

Fig. 1. Cutaway view of geometry of the ACI. The pre-impactor stage and stage 1 are shown without the impactor plates for clarity

to 500 which is below the suggested range of 500–3000 (Marple et al., 2001). Numerous recent studies employ computer simulations to obtain more realistic flow fields, but are primarily dedicated to the case of single-nozzle impactors.

The purpose of this work is to present and justify a reduced model of the ACI, further referred to as the *single jet model*, that can be used to predict and communicate impactor performance. The model is introduced in Section 2 and based on the solution of the Navier–Stokes system for a single jet configuration, with further particle tracking calculations using the previously determined flow field. This procedure is applied to each of the 8 ACI stages. In Section 3, the resulting particle collection efficiency curves and corresponding cutoff diameters are compared with the data found in the literature to check the validity and accuracy of the single jet model at 18, 28.3, and 60 lpm air flow rates. Special attention is given to how gravity should be treated when using a *single jet model* to approximate a multi-nozzle design. Finally, the impactor stage loadings and response functions, obtained using the single jet model, are analyzed in Section 4. These functions are usually employed in the inversion of the impactor data.

2. Methods

2.1. Model formulation

A major challenge in modeling the ACI is the multi-scale nature of the device, as viewed from geometrical and physical perspectives. Indeed, the ratio of the stage plate to the hole diameter can be as large as 2000, and the flow in the impactor appears to be laminar in the initial stages and becomes transitional and then turbulent in the higher stages. The range of the Reynolds numbers based on hole diameter and defined as

$$\mathrm{Re} = \frac{UW}{\nu}, \tag{1}$$

where U is the average nozzle velocity, W is the nozzle diameter, and ν is the air kinematic viscosity, usually varies from 50 in the lower stages up to 2000 in the higher impactors stages. In addition, each ACI stage plate has a large number (up to 400) holes around a millimeter in size.

Despite the increasing power of modern computers, it would be impractical today to try to resolve the flow field in the whole device, or even in a single stage. Therefore, in the present work we analyze each impactor stage individually. As a further necessary simplification, each of the 8 ACI stages are modeled by an averaged single jet impinging on a collecting plate. Furthermore, as the flow rate through the stages increases toward transition/turbulent flows the direct numerical simulation technique used in this work becomes impractical. As such only stages with a Reynolds number under 550 are simulated.

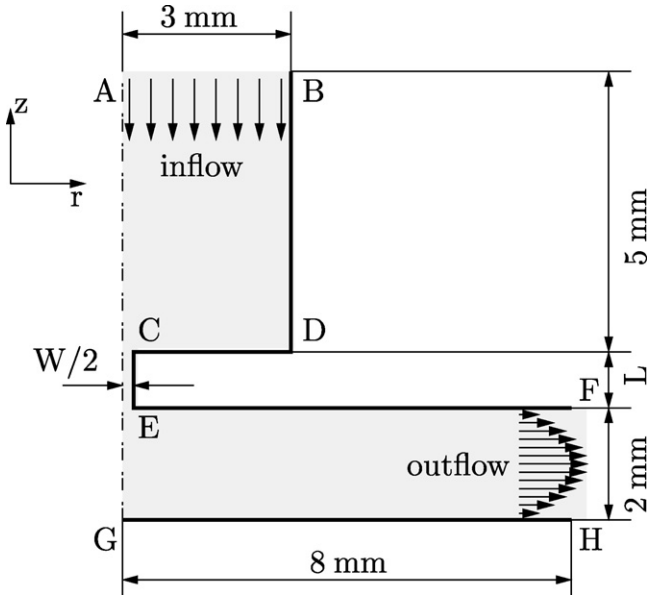

Fig. 2. The schematic of the single stage model used in this study.

Previous theoretical and numerical studies on the effect of gravity in single jet impactors have indicated that the gravitation impaction of the particles cannot be ignored (Huang and Tsai, 2001). However, the geometry of the ACI is significantly different from that of single jet impactors; neighboring jet holes almost certainly have an effect on the flow field in the immediate vicinity of the other jets. Because the role of gravity is not explicitly clear in the ACI, cases will be tested both with and without gravitation impaction and compared with available data.

2.2. Computational model

Fig. 2 shows the two-dimensional axisymmetric configuration in which air with aerosol particles enters the inlet plane AB and then accelerates through the circular nozzle CE. Larger particles with higher inertia impact on the collection plate GH, while smaller ones follow air streamlines more closely and flow out of the domain at the FH plane. Geometric dimensions, specific for each ACI stage such as the hole length and the hole diameter, are given in Table 1; other dimensions are shown in Fig. 2. It should be noted that all these dimensions are consistent with the real geometric parameters of the ACI. The exceptions are the inlet radius AB and the collection plate radius GH that can vary and has to be optimally chosen to simplify the numerical modeling. The inlet radius should not be too large to avoid particle losses due to impaction on the wall CD. The collection plate radius, in principle, has to be close to half of the averaged distance between holes on the ACI stage. It appears, however, that the air flow develops a recirculation zone between planes

Table 1
The ACI nozzle dimensions, shown in Fig. 2.

	Stages							
	0	1	2	3	4	5	6	7
L (mm)	4.1	4.1	1.5	1.55	1.55	1.15	1.15	1.15
W (mm)	2.5	1.8	0.914	0.711	0.533	0.345	0.254	0.254

Table 2
Air flow rates and corresponding jet Reynolds numbers.

Stages	18 lpm		28.3 lpm		60 lpm	
	Hole flow rate ($\times 10^6$ kg/s)	Re	Hole flow rate ($\times 10^6$ kg/s)	Re	Hole flow rate ($\times 10^6$ kg/s)	Re
0	3.828	108.9	12.76	171.2	12.76	363.1
1	3.828	151.3	12.76	237.8	12.76	504.3
2	0.919	71.50	3.063	112.4	3.063	238.3
3	0.919	91.91	3.063	144.5	3.063	306.4
4	0.919	122.6	3.063	192.8	3.063	408.7
5	0.919	190.5	3.063	299.6	–	–
6	0.919	257.3	3.063	404.5	–	–
7	1.828	512.0	–	–	–	–

EF and GH, which must be far enough from the outflow boundary FH in order to properly satisfy the outflow boundary condition. Indeed, the exit flow has to be allowed to leave the computational domain passively without perturbing the upstream flow.

In the present study we employ the Eulerian–Lagrangian model in order to simulate particle-laden air flow in the impactor, as implemented in the ANSYS® Fluent 6.3.26 CFD package. A fundamental assumption made in this model is that the concentration of particles in the air stream is sufficiently dilute (<10% by mass). This assumption permits us to neglect the effects of particle–particle interactions, as well as the effect of particle motion on the air flow. It follows that a one-way coupling prevails; namely the air flow affects particle motion. Thus, the simulation can be performed in two sequential steps by first solving the Navier–Stokes system to obtain the air flow field in the Eulerian coordinate system, then particle trajectories are calculated by solving the equation of particle motion (Lagrangian reference frame) in this flow field.

The governing equations for steady, incompressible axisymmetric air flow without swirl are the continuity

$$\frac{1}{r}\frac{\partial(rv_r)}{\partial r} + \frac{\partial v_z}{\partial z} = 0 \tag{2}$$

and the momentum equations, written in the cylindrical coordinate system

$$\begin{aligned}(\boldsymbol{v}\nabla)v_r &= -\frac{1}{\rho}\frac{\partial p}{\partial r} + \nu\left(\Delta v_r - \frac{v_r}{r^2}\right),\\ (\boldsymbol{v}\nabla)v_z &= -\frac{1}{\rho}\frac{\partial p}{\partial z} + \nu\Delta v_z - g,\end{aligned} \tag{3}$$

where $\boldsymbol{v} = (v_r, v_z)$ and p are the unknown air flow velocity and pressure, respectively. This system is solved using the SIMPLE algorithm with second order spatial discretization. The Gambit mesh generator is employed to create an unstructured triangular computational grid in the domain shown in Fig. 2. The initial mesh is typically refined at least twice to obtain the grid independent solution with the finest grid having about 1.2e5 nodes. The flow simulations are performed for different air flow rates specified on the inlet boundary AB, which are given in Table 2 along with the corresponding Reynolds numbers based on the average jet velocity. Note that the range of Reynolds numbers under consideration corresponds to the laminar flow regime ($\mathrm{Re} \lesssim 550$).

At the outlet plane FH, the pressure outflow boundary condition is imposed by specifying the gauge pressure and the target flow rate. On all other walls the no-slip boundary condition is used.

After obtaining the air flow field, particle trajectories can be calculated by integrating Newton's second law

$$m_p\frac{d\mathbf{v}_p}{dt} = \mathbf{F}_{drag} + m\mathbf{g}, \tag{4}$$

$$\frac{d\mathbf{x}_p}{dt} = \mathbf{v}_p, \tag{5}$$

in which m_p, $\mathbf{v}_p$, and $\mathbf{x}_p$ and are the particle mass, velocity, and position, respectively. The particles are assumed to be rigid and spherical. The right side of (4) is the sum of physically relevant forces acting on a particle, namely the drag force, and the gravitational force. In the simplest form the drag force can be given by the Stokes law

$$\mathbf{F}_{drag} = \frac{3\pi\mu d_p(\boldsymbol{v} - \mathbf{v}_p)}{C_c}, \tag{6}$$

where d_p is the particle diameter, μ is air viscosity, $\boldsymbol{v}$ is the velocity of the air-stream near the particle, and C_c is the Cunningham slip correction factor.

We integrate the equation of particle motion using the variable-order Runge-Kutta scheme, available in Fluent's Discrete Phase Model. The initial positions of the particles are located along the inlet radius AB and their initial velocities are set to zero. The integration of their trajectories continues until the particle impacts or escapes from the computational domain through the outlet FH.

The collection efficiency of the impactor is usually defined as the fraction of particles impacted on the collection plate with respect to to the total number of particles entering the device. Assuming that the particle concentration is uniform at the entrance AB (Fig. 2), the collection efficiency has to be proportional to the entrance area starting from which injected particles are impacted on the plate GH. It can be calculated as

$$\text{collection efficiency} = \left(\frac{r_c}{r_0}\right)^2 \times 100\%, \tag{7}$$

where r_c is the critical particle radial position such that all particles with $r < r_c$ entering the domain would impact on the plate GH, the rest with $r > r_c$ would escape from the computational domain. The radius r_0 corresponds to the initial positions of particles that will enter the jet area and not impact on the plane CD.

3. Results and discussion

Most of the geometric parameters of the single jet model defined in the previous section and shown in Fig. 2 match the corresponding dimensions of the ACI. One important exception is the effective radius of the collection plate GH that, in principle, can vary and affect the particle collection efficiency predicted by the model. Indeed, excessive values of the collection plate radius would result in additional particle impaction due to gravity, especially far from the vicinity of a hole. Such impaction might not take place in the real ACI geometry because of the presence of adjacent holes and cross flow. Therefore, we investigated the influence of gravity on the particle impaction predicted by the single jet model and discuss our results below for two separate cases of computations with and without gravity taken into account.

3.1. Particle impaction without gravity

The calculated collection efficiency curves in the case in which gravity is not taken into account in the equations of the particle motion (4) are shown in Figs. 3–6 and compared with the

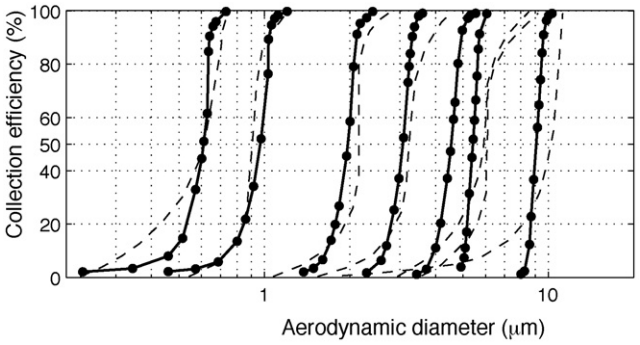

Fig. 3. Computed (solid lines) and measured by Vaughan (1989) (dashed lines) collection efficiency curves for 28.3 lpm air flow rate, without gravity.

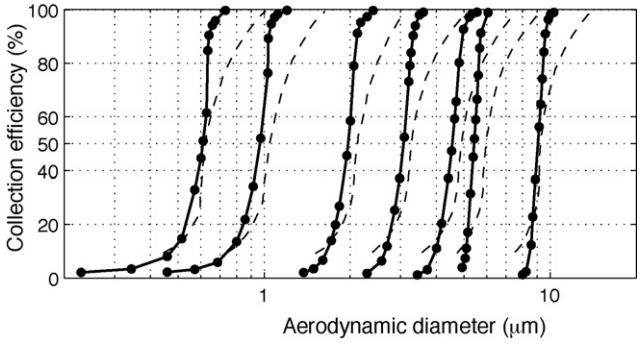

Fig. 4. Computed (solid lines) and manufacturer's calibrated (dashed lines) collection efficiency curves for 28.3 lpm air flow rate, without gravity.

available experimental/calibration data. Fig. 7 compares the model predicted cutoff diameters against the experimental/calibration data. The corresponding cutoff aerodynamic diameters are listed in Table 3.

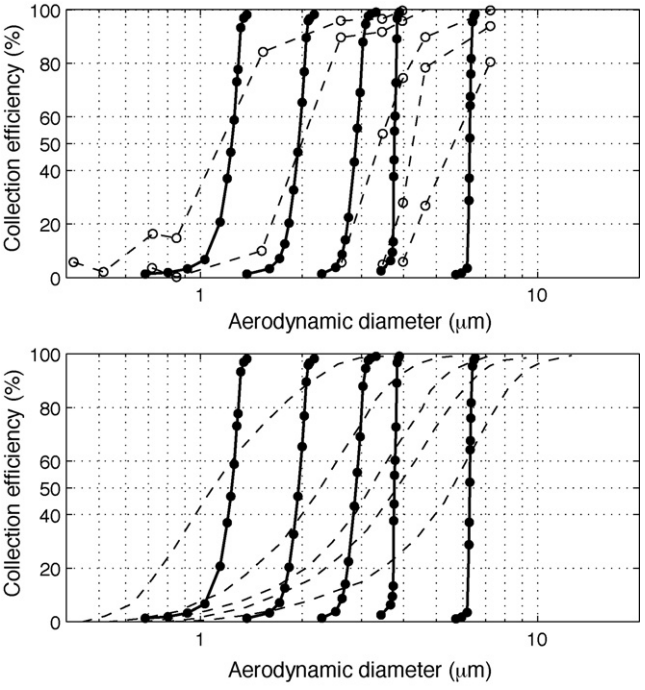

Fig. 5. Computed (solid lines) and measured (dashed lines) collection efficiency curves for 60 lpm air flow rate, without gravity. The measured data is taken from Nichols et al. (1998) (top graph) and Srichana et al. (1998) (bottom graph).

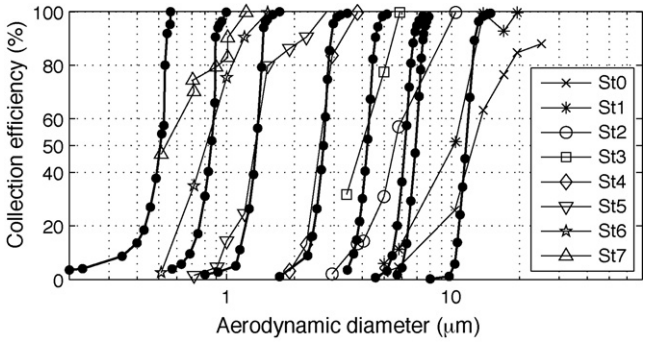

Fig. 6. Computed (solid line) and measured by Zhou et al. (2007) (dashed lines) collection efficiency curves for 18 lpm air flow rate, without gravity.

The collection efficiency curves of the base case of 28.3 lpm air flow rate compare well with the experimental work of Vaughan (1989), as shown in Fig. 3. Working across Fig. 3 from stage 0 to 7 (right to left) stages 0, 1 and 3–6 are in very close agreement with the Vaughan data set. It is interesting to note that the Vaughan data set found the performance of stage 1 and 2 to be nearly identical. While the single hole model does predict the performance of stage 1 and 2 to be similar, the specific overlay of the two stages is not captured by the model.

The base case is in strong agreement with the calibration data from the manufacturer (also supported by Mitchell et al. (1988)) as is evident in Fig. 4. In all cases, the calculated impaction curves appear to be somewhat steeper than the calibration data and the cutoff sizes are in excellent agreement. It should be noted that in nearly all cases, the single hole model does underpredict slightly the impaction size when compared to the experimental data. Reasonable agreement in cutoff size extends up to the 60 lpm air flow rate; unfortunately, a small number of data points combined with combined with probable bounce and re-entrainment effects Nichols et al. (1998), as can be seen in Fig. 5(top graph), which creates some uncertainty about the shape of the corresponding efficiency curves. Another experimental data at 60 lpm is presented in Srichana et al. (1998) (bottom graph), but shows strongly elongated efficiency curves drastically different from those predicted by the single jet model, as well as reported in Nichols et al. (1998). It should be noted that in the Srichana et al. (1998) work a different calibration technique based on an aerodynamic size analyzer was used, which also

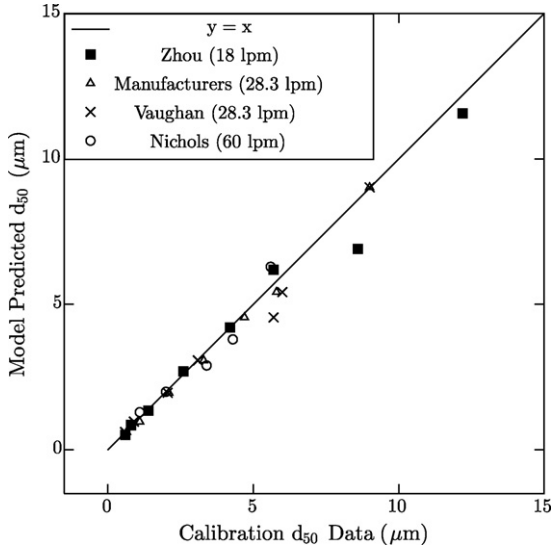

Fig. 7. Q–Q plot of model predicted d_{50} vs. experimental available d_{50}.

Table 3
Cutoff diameters: comparison of experimentally measured with calculated.

Stages	18 lpm		28.3 lpm			60 lpm	
	Zhou et al. (2007)	d_{50} calc.	Manufact. calibration	Vaughan (1989)	d_{50} calc.	Nichols et al. (1998)	d_{50} calc.
0	12.2	11.56	9.0	9.0	9.02	5.6 ±0.3	6.29
1	8.6	6.90	5.8	6.0	5.42	4.3 ±0.3	3.76
2	5.7	6.19	4.7	5.7	4.55	3.4 ±0.2	2.89
3	4.2	4.21	3.3	3.1	3.07	2.0 ±0.1	1.95
4	2.6	2.69	2.1	2.06	1.96	1.1 ±0.1	1.24
5	1.4	1.35	1.1	0.90	0.97	–	–
6	0.8	0.85	0.65	0.60	0.61	–	–
7	0.6	0.51	–	–	–	–	–

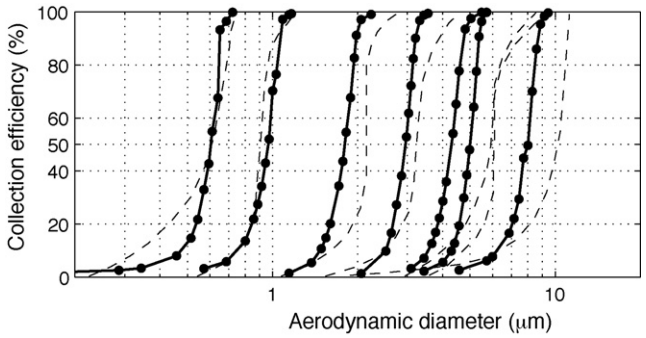

Fig. 8. Computed (solid lines) and measured by Vaughan (1989) (dashed lines) collection efficiency curves for 28.3 lpm air flow rate, with gravity.

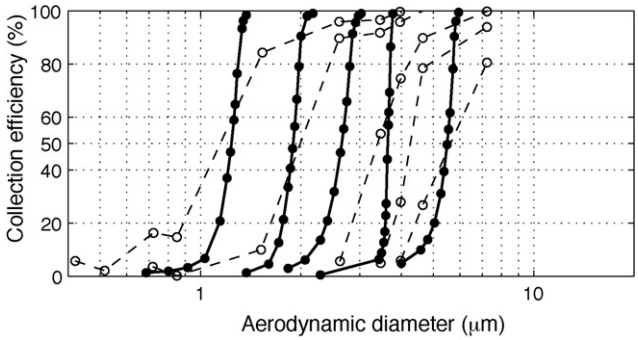

Fig. 9. Computed (solid lines) and measured by Nichols et al. (1998) (dashed lines) collection efficiency curves for 60 lpm air flow rate, with gravity.

produced elongated calibration curves for the base 28.3 lpm case (Srichana et al., 1998). The 28.3 lpm cutoff sizes in the Srichana study were in close agreement with those in the Vaughan and Mitchell work, indicating that the cutoff diameters can be directly compared for this work as well.

Although there is less data available for 18 lpm case, the single hole model cutoff sizes still correlate well to the nebulization data of Zhou et al. (2007).

Overall, the precided cutoff values match well with available experimental data. Fig. 7 is a *Q*–*Q* plot of the predicted d_{50} vs. each of the different experimental data sets. It should be noted that all data sets stay within a fairly tight bound to the $x = y$ line and do not show any detectable trending toward over or under prediction.

3.2. Effect of gravity

When gravity is included in the computation, the overall result is the shifting of the efficiency curves to the left, primarily for the earlier stages/larger particles. For the 28.3 lpm case (Fig. 8) the shift in cutoff diameter for stage 0 and 1 is evident. For stages 2–4 a shift is detectable, however, not to the same extent as in the earlier stages. When the flow rate is increased to 60 lpm a shift is detectable in the early stages, but clearly gravity has less of an effect (Fig. 9).

The shift from the inclusion of gravity tends to give quite a large underprediction of the cutoff size when compared with the experimental data. This contrasts with the case of a single-nozzle impactor, in which models with gravity taken into account allowed better agreement with the experiment.

An explanation for an opposite effect on impaction curves in these cases as attributable to the inclusion of gravity is illustrated in Fig. 10. It shows typical trajectories of particles injected at different radial locations observed at a 28.3 lpm air flow rate for the earlier stages, using the model with gravity included. Particles injected close to the center line would usually impact similarly to particle 1, primarily due to inertia. However, as the location of the particle injection is moved out away from the center line where the entrainment velocity is lower the inertia of the particle lessens. As the inertia decreases, similar sized particles begin to move in the new direction of flow (paths 2–3) and gravity begins to play an important role.

At a certain critical point away from the center line the particle will not impact before a weak reticulation (caused by the flow moving radially away from the hole) will lift the particle upward and it will be allowed to escape (path 5). It is important to note that the radial interval, from which particles are injected and impact due to gravity, is large. Consequently, the collection efficiency increases, respectively. Increasing the flow rate (decreasing particle size) would sharply decrease the radial interval between particle paths 1 and 5 and lower the effect of gravity on the particle impaction as typically observed in the higher ACI stages.

To complete the argument, note that the outlined impaction process most likely would not take place in the multi-hole ACI stage. Indeed, the distance between holes in the ACI is small, and at least

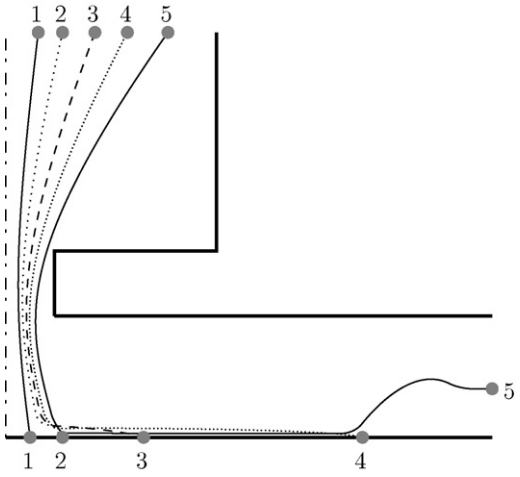

Fig. 10. A sketch of particle trajectories injected at different radial locations; 28.3 lpm air flow rate case with gravity.

two holes should be present on the scale of Fig. 2 to properly conform to the real ACI geometry. As a consequence, the air flow field and particle motion between the nozzle and collection plates will be different from the ones predicted by the single jet model.

It seems, that a way to correct the model in order to avoid this problem would be to make a collection plate GH of a smaller radius, close to the half distance between the holes of the ACI. This modification, however, would complicate the numerical solution and especially the treatment of the outflow boundary condition on plane FH (Fig. 2).

The single jet model clearly has limitations because of its simplicity and, in the present form, can adequately represent only the inertial particle impaction. A fairly good agreement between the experimental data and computations without gravity indicates that in the vicinity of a hole particles indeed impact primarily due to the inertia, especially in the base case 28.3 lpm air flow rate. This also demonstrates the high quality of the ACI design.

4. Stage loadings and impactor stage response functions

As illustrated before, the single jet model provides reasonably accurate estimates of the cutoff diameters, but predicts calibration curves with steeper shapes in comparison with the experimentally measured data. Note that in everyday practice, calibration curves are used directly in the reconstruction of the particle mass/size distribution from gravimetrically measured stage loadings. It is known that such inversion problem is ill-posed. To begin examining this issue, we examine how the uncertainties of the calibration curve shapes affect the stage loadings, which can be calculated assuming that the particle mass/size distribution $P(d_p)$ is provided. Denoting by $S_i(d_p)$ the collection efficiency function for stages $i = 0, 1, \ldots$, the particle mass/size distribution in the air flow leaving the stage i can be found recursively:

$$P_0(d_p) = P(d_p)S_0(d_p), \quad P_1(d_p) = P_0(d_p)S_1(d_p), \quad \ldots \quad ,$$
$$P_i(d_p) = P_{i-1}(d_p)S_i(d_p). \tag{8}$$

Fig. 11 shows such particle size distributions obtained with the calibrated and single jet model collection efficiency functions at 28.3 lpm. For the purposes of the example, the initial distribution of particles entering the impactor is taken as a log-normal, derived from the normal distribution with mean $\mu = 1.44$ and standard deviation $\sigma = 0.94$. As expected, sharper distribution functions are observed for calculated efficiency data. The retained particle mass fraction on each stage is given by the area between adjacent efficiency curves. Shaded areas in Fig. 11, for example, visualize the retained masses on stage 1, which do not look much different for measured and calculated cases.

The corresponding numerical values can be obtained by integration:

$$\begin{aligned} m_0 &= \int [P(d_p) - P(d_p)(1 - S_0(d_p))]dd_p = \int P(d_p)S_0(d_p)dd_p, \\ m_1 &= \int [P(d_p)(1 - S_0) - P(d_p)(1 - S_0(d_p))(1 - S_1(d_p))]dd_p = \\ &\quad \int P(d_p)S_1(d_p)(1 - S_0(d_p))dd_p, \end{aligned} \tag{9}$$

and in general,

$$m_i = \int P(d_p)S_i(D_p)(1 - S_0(d_p))(1 - S_1(d_p)) \ldots (1 - S_{i-1}(d_p))dd_p. \tag{10}$$

For the log-normal initial particle distribution with the parameters given above, these relations predict 30, 9.9, 16, 16, 16 and 4.9% of particles retained on staged 0–5, respectively, when the calibrated

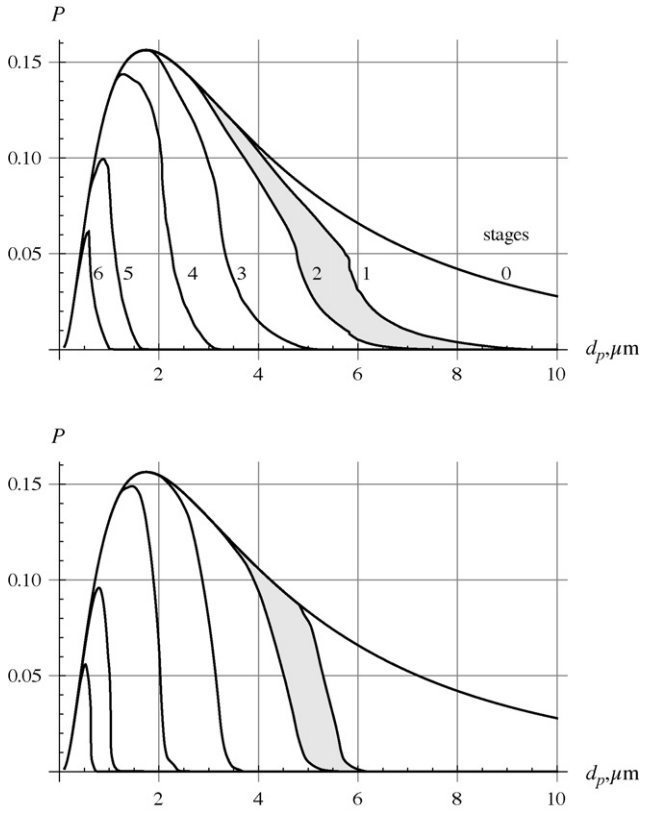

Fig. 11. Particle size distributions for stages from 0 to 6 obtained with the measured (top) and single jet model (bottom) collection efficiency functions at 28.3 lpm.

efficiency data is used. The corresponding values for the calculated efficiency curves are 35, 7.8, 16, 16, 15 and 3.7%. If the particle distribution is uniform on the interval from 0.5 to 9 microns, the stage loadings are 40, 14, 16, 12, 11 and 4.4% for the calibrated and 48, 9.7, 15, 12, 10 and 3.6% for calculated efficiency curves. Clearly, better agreement is observed for the higher impactor stages.

It is also instructive to compare the stage response functions, which are derived from the collection efficiency curves $P_i(d_p)$ and independent of the particle distribution. These functions are usually employed for the inversion of the impactor data (Puttock, 1981). The stage response function is defined as a fraction of all the particles of aerodynamic diameter d_p reaching the impactor, which are collected by that stage. The relations for the stage response functions follow from the formulas for the stage loadings (9) and (10):

$$\begin{aligned} R_0(d_p) &= S_0(d_p), \\ R_i(d_p) &= S_i(d_p)\prod_{j=0}^{i-1}[1 - S_j(d_p)], \end{aligned} \tag{11}$$

so that retained masses can be calculated as

$$m_i = \int P(d_p)R_i(d_p)dd_p. \tag{12}$$

Alternatively, the recursive formula for the response functions (Puttock, 1981) is given as

$$R_i(d_p) = S_i(d_p)\left[1 - \sum_{j=0}^{i-1} R_j(d_p)\right]. \tag{13}$$

For the ideal impactor stage i that collects all particles above a certain size $d_{50,i}$ the response functions are "top-hat" functions equal to 1 for $d_{50,i} < d_p < d_{50,i-1}$ and zero elsewhere. In reality,

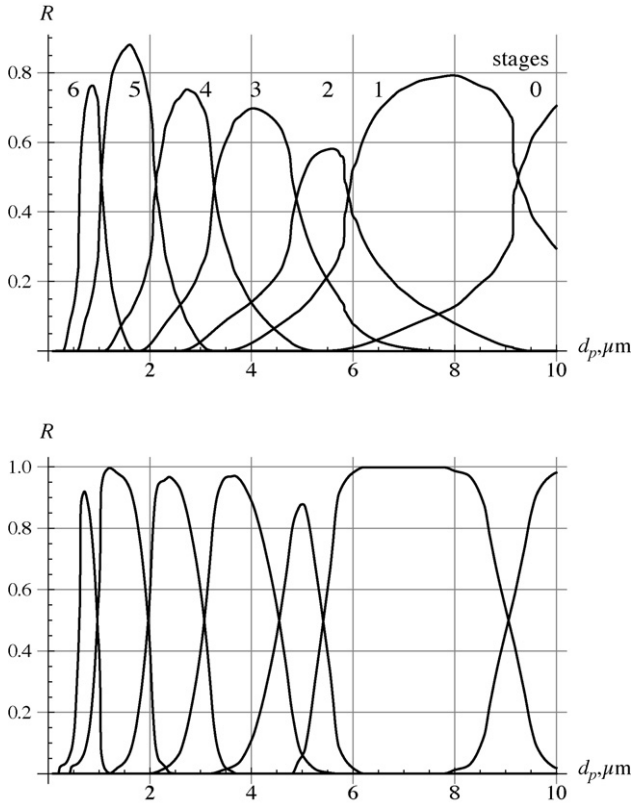

Fig. 12. Calibrated (top) and calculated (bottom) impactor stage response functions at 28.3 lpm air flow rate.

the response functions for stages 1 and higher are bell-shaped, due to the finite slope of the collection efficiency curves. Fig. 12 shows the impactor response functions plotted for the experimentally calibrated (top) and calculated using the single jet model (bottom) collection efficiency functions at 28.3 lpm air flow rate.

The calibrated responses are far from ideal and always < 1 because of the strong overlap of the corresponding efficiency curves. In contrast, the shape of the calculated curves is steeper, with the values of the response functions close to 1 in the vicinity of their peaks.

5. Summary

The purpose of this study was to present and evaluate a reduced single jet model of the Andersen cascade impactor that allows efficient performance characterization of the device. In this model, the multiple-hole impactor stage was represented by a single jet impinging on a collection plate and particle tracking was performed in the viscous flow field obtained from the numerical simulations. Therefore, it can be viewed as a compromise between simplified analytical models and possible models in which multi-hole impactor stage geometry is involved. In the former case, the air flow field is assumed to be potential, thus neglecting the effect of the viscous boundary layer on particle motion. The numerical resolution of the 3D flow field in a multi-hole stage, however, is prohibitively expansive even in the laminar regime.

The model was applied to obtain the collection efficiency curves at 18, 28.3, and 60 lpm air flow rates. The comparison with the corresponding experimental data demonstrates good agreement for the predicted cutoff diameters. Our results also indicate that the single jet model can provide reasonably accurate estimates of the impactor stage loadings. The shape of the efficiency curves, however, is observed to be sharper in comparison with the experimentally calibrated data. This fact can be attributed to the adjacent jets interaction and cross-flow effects that are not taken into account by the current single jet model. Further studies are needed to incorporate appropriate corrections into the model, as well as to examine the wall losses and the effect of particle bounce on the shape of the efficiency curves.

Nevertheless, the main advantage of the single jet model is that it is simple, computationally efficient, and in the present form, can be easily adopted to the analysis of the ACI performance and data inversion.

References

Davies, C.N., Alyward, M., 1951. The trajectories of heavy, solid particles in a two-dimensional jet of ideal fluid impinging normally upon a plate. Proc. Phys. Soc. (Lond.) B64, 889–911.
Huang, C.-H., Tsai, C.-J., 2001. Effect of gravity on particle collection efficiency of inertial impactors. Aerosol Sci. 32, 375–387.
Marple, V.A., Olson, B.A., Rubow, K.L., 2001. Inertial, gravitational, centrifugal, and thermal collection techniques. In: Willeke, K., Baron, P.A. (Eds.), Aerosol Measurement: Principles, Techniques, and Applications. Wiley.
Marple, V.A., Willeke, K., 1976. Impactor design. Atmos. Environ. 10, 891–896.
May, K.R., 1945. The cascade impactor: an instrument for sampling coarse aerosols. J. Sci. Instrum. 22, 187–195.
Mercer, T.T., Stafford, R.G., 1968. Impaction from round jets. Ann. Occup. Hyg. 12, 41–48.
Mitchell, J.P., Costa, P.A., Waters, S., 1988. An assessment of an Andersen Mark-II cascade impactor. J. Aerosol Sci. 19, 213–221.
Nichols, S.C., Brown, D.R., Smurthwaite, M., 1998. New concept for the variable flow rate Andersen cascade impactor and calibration data. J. Aerosol Med. 11, 133–138.
Puttock, J.S., 1981. Data inversion for cascade impactors: fitting sums of log-normal distributions. Atmos. Environ. 15, 1709–1716.
Ranz, W.E., Wong, J.B., 1952. Impaction of dust and smoke particles. Ind. Eng. Chem. 44, 1371–1381.
Srichana, T., Martin, G.P., Marriott, C., 1998. Calibration method for the Andersen cascade impactor. J. Aerosol Sci. 29, 761–S762.
Vaughan, N.P., 1989. The Andersen impactor: calibration, wall losses and numerical simulation. J. Aerosol Sci. 20, 213–221.
Zhou, Y., Brasel, T.L., Kracko, D., Cheng, Y., Ahuja, A., Norenberg, J.P., Kelly, H.W., 2007. Influence of impactor operating flow rate on particle size distribution of four jet nebulizers. Pharm. Dev. Technol. 12, 353–359.